Universal Scaling Laws for Nose Bluntness Effects on Hypersonic Unsteady Aerodynamics

LARS ERIC ERICSSON*
Lockheed Missiles & Space Company, Sunnyvale, Calif.

The hypersonic aerodynamic characteristics of pointed bodies of revolution are relatively well understood and can be predicted theoretically, at least as long as the viscous effects are not large. No such satisfactory conditions exist for blunted bodies of revolution, especially not in regard to the bluntness induced effects on the vehicle dynamics. Embedded Newtonian flow concepts and hypersonic similitude are used to develop universal scaling laws that can predict the nose-bluntness induced effects on the hypersonic characteristics of slender bodies of revolution. The derived scaling laws are found to collapse the limited experimental data available. The laws permit one set of test data, or theoretically derived characteristics, to be extrapolated to predict the nose-bluntness induced effects for another configuration in the same geometric family, e.g., blunted cones and blunt cylinder-flare bodies. The derived scaling laws, when combined with existing pointed body theories, should provide the capability to predict the hypersonic unsteady aerodynamic characteristics of most blunted slender bodies of revolution of current interest.

Nomenclature

ΔA	= surface area element, m²
c	= reference length, m (cylinder caliber or cone base diameter, d_B)
d_B	= base diameter, m
d_N	= nose (bluntness) diameter, m
D_N	= nose drag; coefficient $C_{D_N} = D_N/(\rho_\infty U_\infty^2/2)(\pi d_N^2/4)$
f	= dynamic pressure ratio, $f = \rho U^2/\rho_\infty U_\infty^2$
g	= velocity ratio, $g = U/U_\infty$
l and l_0	= geometric length dimensions (see Figs. 2 and 3)
p	= static pressure kg/m², coefficient $C_p = (p - p_\infty)/(\rho_\infty U_\infty^2/2)$
q	= rigid body pitch rate, radians/sec
r	= body radius, m (see Fig. 1)
R	= radial distance from bow shock centerline, m (see Fig. 1)
R_{sh}	= bow shock radius, m
S	= reference area, m² ($S = \pi c^2/4$)
t	= time, sec
U	= axial velocity, m/sec
x	= axial coordinate (see Fig. 1)
$\Delta\bar{x}$	= cone c.g. coordinate (see Fig. 3)
α	= angle of attack, radians or degrees
δ^*	= boundary-layer displacement thickness, m
Δ	= difference or increment
$\eta = r/c$	= dimensionless radius
θ	= surface slope, radians or degrees (see Fig. 1)
$\xi = x/c$	= dimensionless axial coordinate
ρ	= air density, kg sec²/m⁴
σ	= radial distance ratioed to shock radius, $\sigma = R/R_{sh}$
χ_l and χ_{l_0}	= hypersonic correlation parameter, Eq. (15)
ω	= pitch frequency, radians/sec

Subscripts

B	= base
c	= cone
c.g.	= center of gravity or oscillation center
F	= flare
max	= maximum or stagnation value
L	= local instantaneous force
N	= nose
sh	= bow shock
0	= at bow shock centerline
∞	= freestream conditions or Newtonian values

Superscripts

i	= induced, e.g., $\Delta^i C_m$ = nose bluntness induced pitching moment coefficient

Derivative symbols

C_{m_α}	= $\partial C_m/\partial\alpha$
C_{m_q}	= $\partial C_m/\partial(cq/U_\infty)$
$C_{m_{\dot\alpha}}$	= $\partial\Delta^i C_m/\partial(c\dot\alpha/U_\infty)$
$C_{m_q} + C_{m_{\dot\alpha}}$	= $\partial C_m/(cq\partial/U_\infty) + \partial\Delta^i C_m/\partial(c\dot\alpha/U_\infty)$
$\dot\alpha$	= $\partial\alpha/\partial t$

Presented as Paper 68-1158 at the AIAA Entry Vehicle Systems and Technology Meeting, Williamsburg, Va., December 3–5, 1968; submitted December 12, 1968; revision received May 1, 1968.

* Senior Staff Engineer, Flight Technology. Associate Fellow AIAA.

Introduction

BLAST wave similitude of hypersonic nose bluntness effects has long been established.[1,2] Blunted cone pressures are well correlated using Cheng's similarity parameter.[2,3] Walchner and Clay[4] concluded that the integrated aerodynamic loads should also be correlated if the blunted cone body length was chosen as the reference length. They could not, however, theoretically account for the experimentally observed dynamic stability trends for reasons that become evident when the nose bluntness induced entropy wake effects are correctly accounted for.[5–7]

Embedded Newtonian flow concepts are used in the present paper to derive the nose-bluntness induced effects on the static and dynamic stability of slender bodies of revolution. It is shown how a universal scaling of the ratio between blunt and sharp body stability characteristics can be accomplished. The derived scaling laws collapse theoretical and experimental data for 5.6° and 10° half-angle blunted cones to one (preliminary design) curve.

Analysis

Seiff's embedded Newtonian flow concept[8] is described by Eq. (1). In past applications of this concept by Seiff and others the effects of translating a body element in the entropy gradient field were neglected. Thus, for the α derivative

$$\frac{\partial C_p}{\partial\alpha} = \frac{\partial C_{p0}}{\partial\alpha} + \frac{\rho U^2}{\rho_\infty U_\infty^2}\frac{\partial C_{p\text{Newt}}}{\partial\alpha} + C_{p\text{Newt}}\frac{\partial}{\partial\alpha}\left(\frac{\rho U^2}{\rho_\infty U_\infty^2}\right)$$

the last term was neglected. It can be shown[6] that this was

justified for very blunt cylinder flare bodies at $\alpha = 0$. However, at angles of attack where the flare will protrude into the high-entropy gradient region the effects are no longer small.[9] In the case of dynamic stability derivatives the finite time lag occurring before the nose translation has resulted in a translation of the nose (blast wave) generated flowfield at the flare must also be accounted for.[5] For moderate nose bluntnesses this unsteady embedded-Newtonian theory can also be applied to a slender cone.[7] Equation (1) defines the pressure coefficient on a body element ΔA embedded in a nonuniform flowfield (Fig. 1);

$$C_p = C_{p_0} + (\rho U^2/\rho_\infty U_\infty^2)(C_p)_{\text{Newt}} \tag{1}$$

C_{p_0} is the static pressure in absence of a flare (the blast wave pressure). The dynamic pressure ratio $\rho U^2/\rho_\infty U_\infty^2$ is in general a function of both x/d_N and R/R_{sh}. If one excludes the near nose region, these two-parameter entropy profiles can be simplified to one-parameter profiles. Thus, using similar flow profiles, the dynamic pressure ratio well downstream of the nose can be defined as

$$\rho U^2/\rho_\infty U_\infty^2 = f(\sigma); \quad \sigma = R/R_{sh} \tag{2}$$

The shock radius R_{sh} is determined by the nose drag[9]

$$R_{sh}/d_N = 1.0 C_{D_N}^{1/4}[(x - x_{sh})/d_N]^{1/2} \tag{3}$$

where $x_{sh} \approx x_N$.

At $\alpha = 0$,† when $R = r$ (Fig. 1), R/R_{sh} becomes simply

$$R/R_{sh} = C_{D_N}^{-1/4}(r/d_N)(x/d_N - x_{sh}/d_N)^{-1/2} \tag{4}$$

For a flare not near the nose,

$$(x_{sh}/C_N)^2 \ll (x/d_N)^2$$

and $(R_{sh}/R)^2$ can be written

$$(R/R_{sh})^2 = C_{D_N}^{-1/2}(r_B/d_N)^2(r/r_B)^2(x/d_N)^{-1} \tag{5}$$

The ratio between the forces on the surface element ΔA in embedded Newtonian and pure Newtonian flow is for similar profiles determined by R/R_{sh}. The parabolic shape

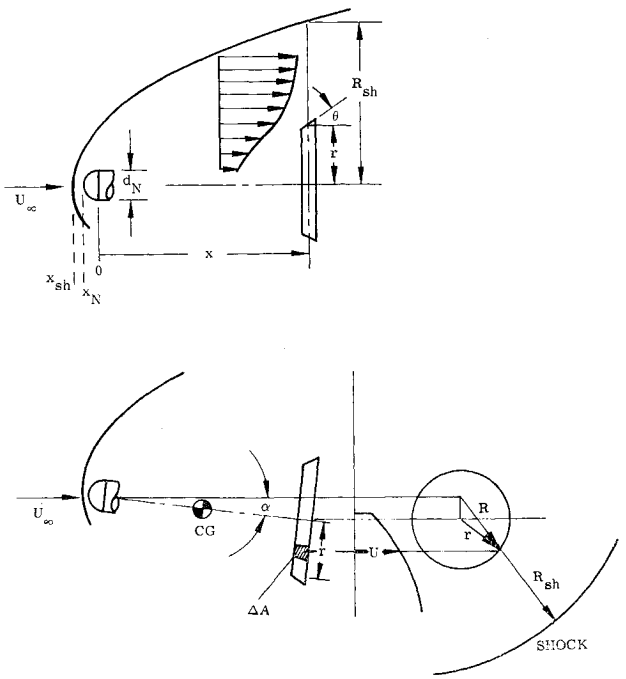

Fig. 1 Bow shock-induced inviscid shear flow at near zero angle of attack.

† Only stability derivatives at $\alpha = 0$ are considered in the present paper.

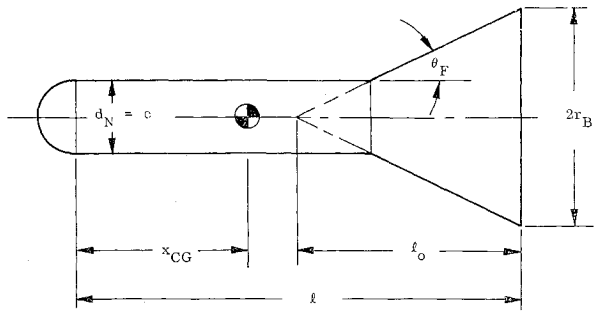

Fig. 2 Flared body geometry.

of the dynamic pressure profile makes $(R/R_{sh})^2$ a logic similarity parameter. Using Fig. 2, the hypersonic similarity parameter can be defined as follows:

$$(R/R_{sh})^2 = \chi_l(r/r_B)^2(x/l)^{-1} \tag{6}$$

where

$$\chi_l = C_{D_N}^{-1/2}(r_B/d_N)(r_B/l) \tag{6a}$$

and

$$r/r_B = 1 - (l/l_0)(1 - x/l) \tag{6b}$$

The contributions of the flare in Fig. 2 to static and dynamic stability as defined by Embedded Newtonian theory[6] can be formulated as follows for $\alpha = 0$:

$$\left.\begin{aligned} (C_{m\alpha})_F &= C_{m\alpha_L} + \Delta^i C_{m\alpha} \\ C_{m\alpha_L} &= -8C_{p_{\max}} \cos^2\theta_F \left(\frac{2}{\sin 2\theta_F}\right) \int_{\eta_1}^{\eta_2} (\Delta_0 + \eta) f \eta \, d\eta \\ \Delta^i C_{m\alpha} &= -4C_{p_{\max}} \cos^2\theta_F \times \\ &\quad \left(\frac{2}{\sin 2\theta_F}\right) \int_{\eta_1}^{\eta_2} (\Delta_0 + \eta)(\Delta_1 + \eta) \frac{\partial f}{\partial \eta} \eta d\eta \end{aligned}\right\} \tag{7}$$

$$\left.\begin{aligned} (C_{m_q} + C_{m\dot{\alpha}})_F &= C_{m_q} + C_{m\dot{\alpha}} \\ C_{m_q} &= -8C_{p_{\max}} \cos^2\theta_F \left(\frac{2}{\sin 2\theta_F}\right)^2 \times \\ &\quad \int_{\eta_1}^{\eta_2} (\Delta_0 + \eta)^2 \frac{f}{g} \eta d\eta \\ C_{m\dot{\alpha}} &= 4\xi_{CG} C_{p_{\max}} \cot\theta_F \int_{\eta_1}^{\eta_2} (\Delta_0 + \eta) \times \\ &\quad (\Delta_1 + \eta)\left(\frac{1}{g}\right)\left(\frac{\partial f}{\partial \eta}\right) \eta \, d\eta \end{aligned}\right\} \tag{8}$$

where

$$\left.\begin{aligned} c\Delta_0 &= (l - l_0 - x_{CG}) \sin\theta_F \cos\theta_F \\ c\Delta_1 &= c\Delta_0 \cos^{-2}\theta_F + x_{CG} \tan\theta_F \end{aligned}\right\} \tag{9}$$

The ratios between the stability derivatives in embedded Newtonian ($f \neq 1$, $g \neq 1$) and pure Newtonian theory ($f = g = 1$) are

$$\left.\begin{aligned} C_{m\alpha}/C_{m\alpha_\infty} &= C_{m\alpha_L}/C_{m\alpha_\infty} + \Delta^i C_{m\alpha}/C_{m\alpha_\infty} \\ \frac{C_{m\alpha_L}}{C_{m\alpha_\infty}} &= \int_{\eta_1}^{\eta_2} (\Delta_0 + \eta) f \eta \, d\eta \Big/ \int_{\eta_1}^{\eta_2} (\Delta_0 + \eta)\eta \, d\eta \\ \frac{\Delta^i C_{m\alpha}}{C_{m\alpha_\infty}} &= \frac{1}{2}\int_{\eta_1}^{\eta_2} (\Delta_0 + \eta)(\Delta_1 + \eta) \frac{\partial f}{\partial \eta} \eta d\eta \Big/ \\ &\quad \int_{\eta_1}^{\eta_2} (\Delta_0 + \eta)\eta \, d\eta \end{aligned}\right\}$$

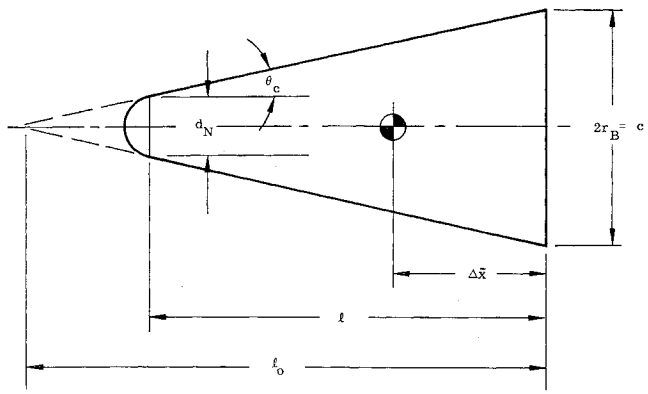

Fig. 3 Blunted cone geometry.

$$\left.\begin{aligned}(C_{mq} + C_{m\dot{\alpha}})/C_{mq_\infty} &= C_{mq}/C_{mq_\infty} + C_{m\dot{\alpha}}/C_{mq_\infty}\\ \frac{C_{m_\sigma}}{C_{mq_\infty}} &= \int_{\eta_1}^{\eta_2}(\Delta_0+\eta)^2\frac{f}{g}\,\eta d\eta \Big/ \int_{\eta_1}^{\eta_2}(\Delta_0+\eta)^2\,\eta d\eta\\ \frac{C_{m\dot{\alpha}}}{C_{mq_\infty}} &= -\frac{\xi_{CG}}{4}\sin 2\theta_F \int_{\eta_1}^{\eta_2}(\Delta_0+\eta)\times\\ &\quad (\Delta_1+\eta)\frac{1}{g}\frac{\partial f}{\partial \eta}\,\eta d\eta \Big/ \int_{\eta_1}^{\eta_2}(\Delta_0+\eta)^2\eta\eta d\end{aligned}\right\} \quad (11)$$

If $(R/R_{sh})^2$ is simulated, f and g are also simulated and the stability ratios above, Eqs. (10) and (11), will remain constant if

$$\left.\begin{aligned}\xi_{CG}\sin 2\theta_F &= \text{const}\\ (\Delta_1+\eta)/(\Delta_0+\eta) &= \text{const}\end{aligned}\right\} \quad (12)$$

When θ_F is small, Eqs. (9) and (12) give

$$\left.\begin{aligned}\xi_{CG}\theta_F &= \text{const}\\ \frac{\Delta_1+\eta}{\Delta_0+\eta} = 1 + \frac{\xi_{CG}\theta_F}{\Delta_0+\eta} &= \text{const}\end{aligned}\right\} \quad (13)$$

Equation (13) is essentially satisfied if $\xi_{c.g.}\theta_F$ remains constant, as Δ_0 usually is small compared to η. For a statically stable vehicle with a slender flare, the variation of Δ_0 will cause less than 10% variation in $(\Delta_1+\eta)/(\Delta_0+\eta)$. Equation (6) says that θ_F essentially determines only how fast $(R/R_{sh})^2$ changes with x, whereas the integrated flare force is determined by χ_l alone. The lever arms for the flare forces will vary somewhat with θ_F. However, the stability ratios in Eqs. (10) and (11) are not critically dependent upon the lever arms as the center of pressure difference between embedded Newtonian and Newtonian flare forces is negligible compared to a realistic lever arm. This is true even when the c.g. ($x_{c.g.}$) approaches the flare, as has been shown in a comparison between quasi-steady and embedded Newtonian results.[6]

Consequently, the nose bluntness induced effects on a flare $(C_{m\alpha} + \Delta^i C_{m\alpha})/(C_{m\alpha_\infty}$ and $(C_{mq} + C_{m\dot{\alpha}})/C_{mq_\infty}$ are scaled if

$$\left.\begin{aligned}\chi_l = C_{DN}^{-1/2}(r_B/d_N)(r_B/l) &= \text{const}\\ \xi_{c.g.}\theta_F &= \text{const}\end{aligned}\right\} \quad (14)$$

χ_l is essentially Cheng's similarity parameter[2] for the body trailing edge, and it assures the scaling of the local flare forces necessary for scaling of $C_{m\alpha_L}/C_{m\alpha_\infty}$ and C_{mq}/C_{mq_∞}. The second requirement, $\xi_{c.g.}\theta_F$ = constant, states the fact that the effect of entropy gradient[5,6] is larger the steeper the flare is, i.e., the faster the cross-sectional area changes with x. Its scaling assures the scaling of $\Delta^i C_{m\alpha}/C_{m\alpha_\infty}$ and $C_{m\dot{\alpha}}/C_{mq_\infty}$. Because the flare is usually not near the body c.g. $\xi_{c.g.}$ can be varied to satisfy the requirement of constant $\xi_{c.g.}\theta_F$. The resultant changes of the flare force lever arms will not appreciably affect the stability ratios, Eqs. (10) and (11), as was pointed out earlier.

For a conical body, however, this variation in lever arms is no longer negligible, and it appears that the two scaling requirements in Eq. (14) cannot be satisfied simultaneously. Fortunately, this pessimistic outlook for scaling of cone bluntness effects proves to be false.

With the definitions in Fig. 3, the scaling requirements can be derived from Eqs. (6) and (13) to give the following:

$$\left.\begin{aligned}\chi_l &= \chi_{l_0}(1 + d_N/d_B)^{-1}\\ \chi_{l_0} &= C_{DN}^{-1/2}(r_B/d_N)(r_B/l_0)\end{aligned}\right\} \quad (15)\ddagger$$

$$\left.\begin{aligned}\xi_{c.g.}\theta_F &= (\tfrac{1}{2})[1 - (\Delta\bar{x}/l_0) - (d_N/d_B)]\\ \frac{\Delta_1+\eta}{\Delta_0+\eta} &= \frac{\eta - (1/2)(d_N/d_B)}{\eta - 1/2(1 - \Delta\bar{x}/l_0)}\end{aligned}\right\} \quad (16)$$

Noticing with Wagner and Watson[3] that the correlation of cone pressures is equally good whether or not x_s in Eq. (4)

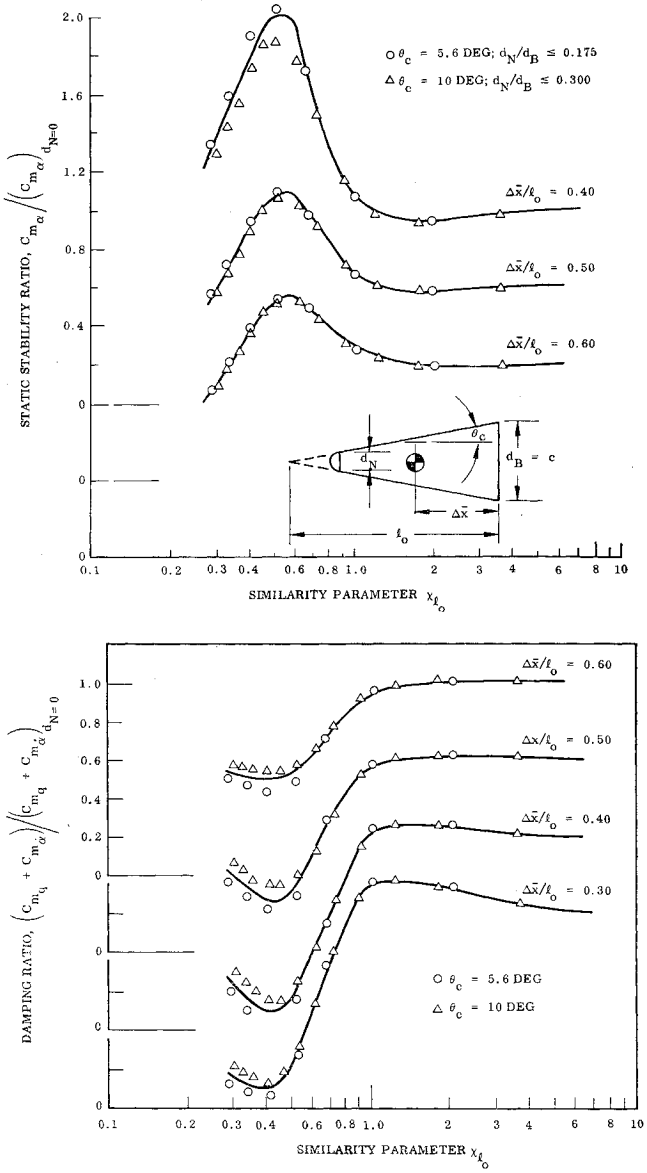

Fig. 4 Scaling of theoretical results on slender blunted cones.

‡ χ_l is related to Walchner and Clay's correlation parameter C. For $C_{DN} = 1$ and $l + d_N/2 \approx l$, $\chi_l \approx C^2$.

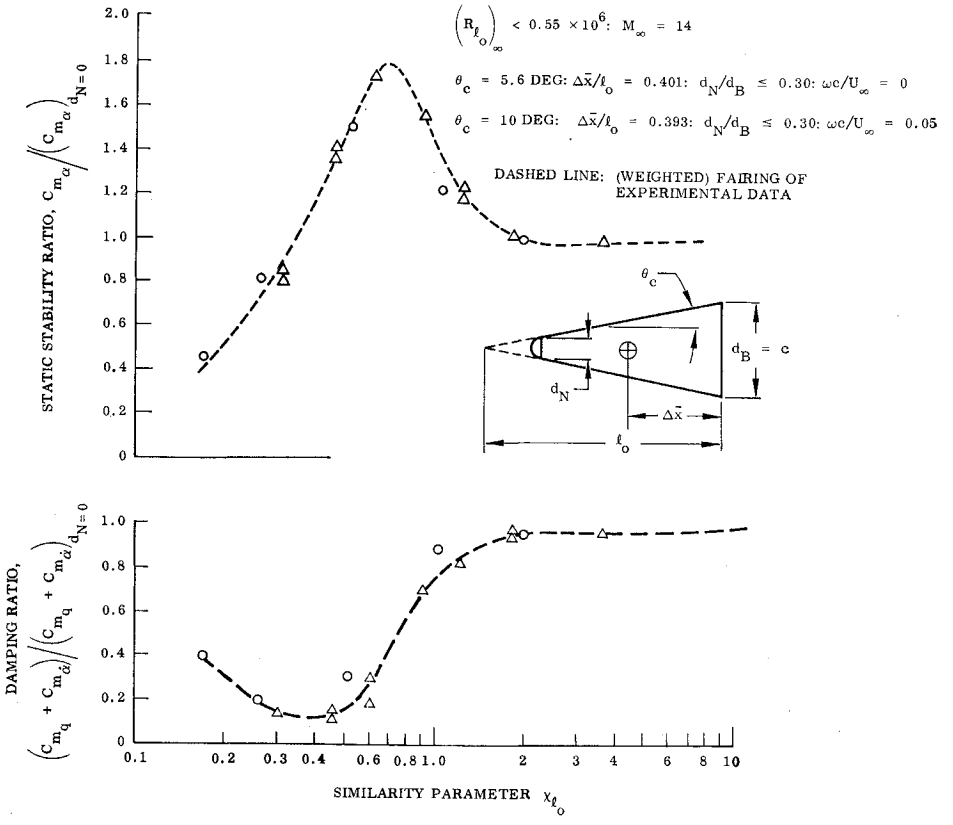

Fig. 5 Scaling of experimental data for slender blunted cones.

is chosen as $x_s = -d_N/2$ or $x_s = 0$ one would expect that χ_{l_0} in Eq. (15) could well represent χ_l, at least for small nose-bluntness (d_N/d_B). For the same reason, neglecting small differences in nose-bluntness (d_N/d_B) in Eq. (16) would be permissible. Thus, the scaling of the effects of small nose-bluntness on a conical frustum should be assured by

$$\left.\begin{aligned}\chi_{l_0} = C_{D_N}{}^{-1/2}(r_B/d_N)(r_B/l_0) &= \text{const}\\ (\Delta\bar{x}/l_0) &= \text{const}\end{aligned}\right\} \tag{17}$$

Equation (17) is valid only for small nose-bluntness, in which case the effects of the nose tip loads can be neglected. That is, Eq. (17) should scale the stability ratios between moderately blunt and sharp cones.

Discussion

The derived scaling laws are very simple and will, if proven correct, greatly simplify the preliminary design of high performance re-entry vehicles. The scaling of the flared body

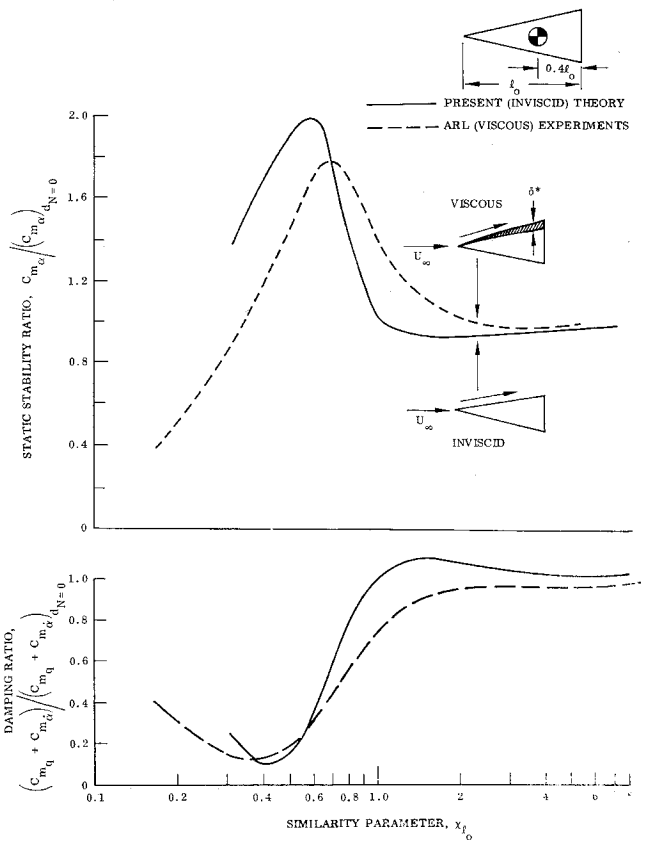

Fig. 6 Comparison between inviscid theory and viscous experiment.

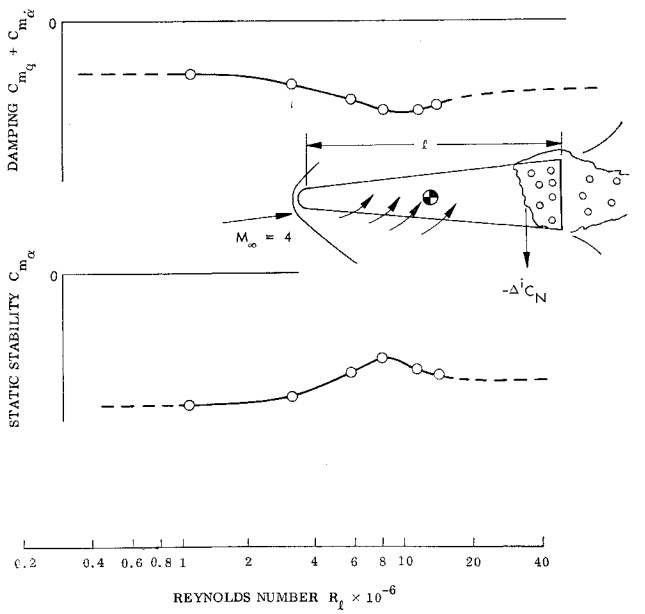

Fig. 7 Effect of Reynolds number on cone stability derivatives at $M_\infty = 4$.

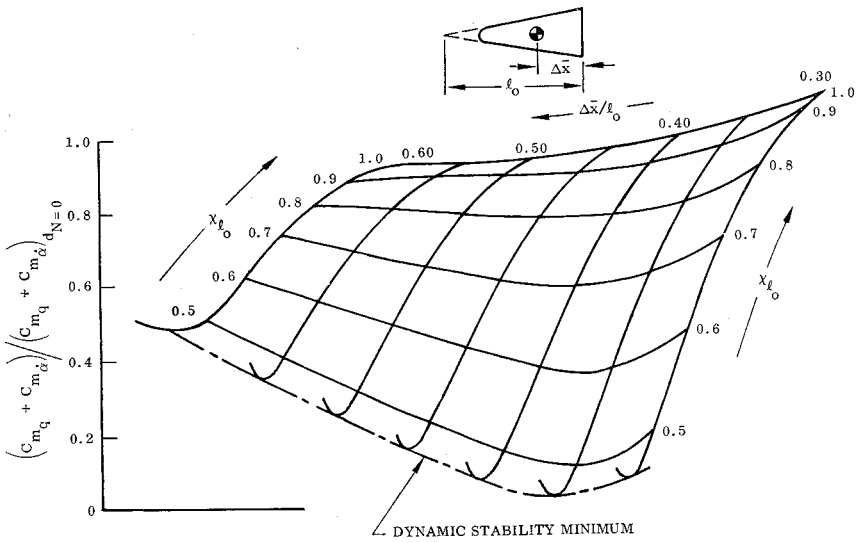

Fig. 8 Effect of center of gravity and hypersonic similarity parameter on dynamic stability of slender blunted cones.

stability is rather straightforward. It is the cone scaling that needs an acid test. This is especially true in view of the fact that the slender blunted cone is the re-entry body geometry of current interest.

By ratioing the experimental blunted cone data to the pointed cone data viscous (boundary-layer cross flow) effects common to both the blunted and sharp cone are eliminated. Thus, the experimental stability ratio can be expected to scale as well as the inviscid theoretical stability ratio as long as the nose bluntness does not have a large influence on the viscous effects. The latter would tend to be the case if boundary-layer transition does not occur on the (aft) body.[10]

Figure 4 shows that the simple analytic theory[7] derived from the embedded Newtonian concepts[5,6] supports the scaling laws derived here.

The cone semi-angles, $\theta_c = 5.6°$ and $\theta_c = 10°$, were not selected at random but are the angles used by Clay and Walchner in a systematic series of wind-tunnel tests.[4,11] The present scaling laws are seen to collapse the experimental data to one curve (Fig. 5). The slight difference in c.g. location has negligible effect on the stability ratios (see Fig. 8). The fairing is weighted toward the 10° cone data in an attempt to correct for the relatively larger viscous effects on the more slender 5.6° cone. The difference between the predicted inviscid stability ratios and those measured experimentally on bodies with relatively thick laminar boundary layers are to be expected (Fig. 6). The apparent nose-bluntness due to viscosity will give lower effective values of the similarity parameter (χ_{l_0}) than the inviscid values used.

It should be emphasized that good scaling of experimental nose-bluntness effects using the present scaling laws can be expected only as long as boundary layer transition does not occur on the conical frustum. When it does, large effects of Reynolds number have been measured[11,12] (Fig. 7). The appreciable effects of boundary-layer transition at supersonic speeds can be expected to increase greatly at hypersonic speeds and to be coupled with the nose bluntness induced effects.[13,14]

Figure 8 is a carpet plot[15] of the dynamic stability ratio as a function of c.g. location ($\Delta\bar{x}/l_0$) and similarity parameter χ_{l_0}. It appears that the dynamically destabilizing effects of nose bluntness will be maximum for a typical c.g. location, $0.30 < \Delta\bar{x}/l_0 < 0.40$.

For hemispherical nose bluntness, almost total loss of dynamic stability is obtained for $\Delta\bar{x}/l_0 = 0.35$ (Fig. 9). The critical χ_{l_0} value giving minimum dynamic stability in the cg range of interest, $0.25 < \Delta\bar{x}/l_0 < 0.50$ is $\chi_{l_0} = 0.455$ (Fig. 9) giving the critical nose bluntness $(d_N/d_B)_{\text{crit}} \approx 0.0209\ \theta_c$ deg (Fig. 10).

Conclusions

Using embedded Newtonian flow concepts universal scaling laws for hypersonic nose-bluntness effects have been derived for cylinder-flare bodies and slender cones. The derived scaling laws collapse theoretical and experimental data for slender cones with 5.6- and 10° half-angles and bluntness ratios up to 30%. High Reynolds number experiments giving turbulent boundary layer§ on slender blunted cones

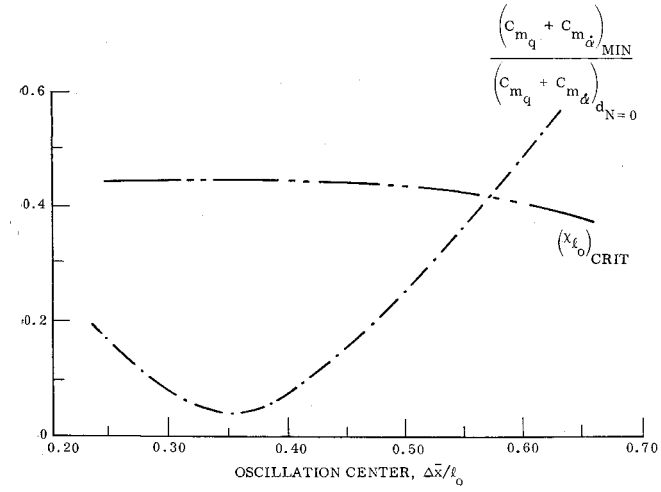

Fig. 9 Minimum dynamic stability of slender cones.

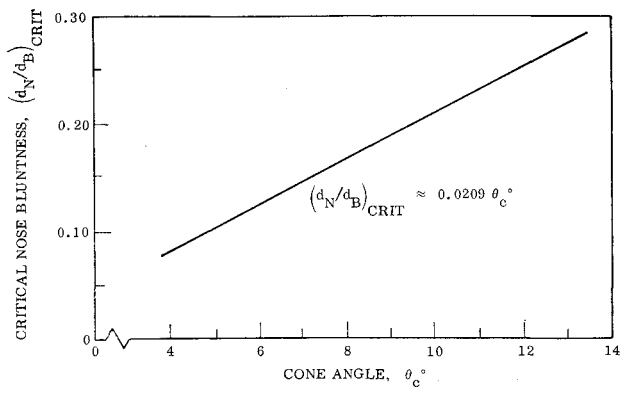

Fig. 10 Spherical nose bluntness giving minimum dynamic stability for slender cones.

§ Over all but the near nose region.

are needed to check out the derived inviscid scaling laws. Examination of the deviations between viscous experimental data presently available and the theoretical predictions gives one reason to believe that the derived scaling laws will prove to be correct. The scaling laws, when combined with existing pointed body or Newtonian theories, provide the capability to predict the hypersonic unsteady aerodynamic characteristics of most re-entry bodies of current interest.

References

[1] Hayes, W. D. and Probstein, R. F., *Hypersonic Flow*, Academic Press, New York, 1959.

[2] Cheng, H. K., "Similitude of Hypersonic Real-Gas Flows over Slender Bodies with Blunted Noses," *Journal of the Aerospace Sciences*, Vol. 26, 1959, pp. 575–585.

[3] Wagner, R. D., Jr. and Watson, R., "Induced Pressures and Shock Shapes on Blunt Cones in Hypersonic Flow," TND 2182, March 1964, NASA.

[4] Walchner, O. and Clay, J. T., "Nose Bluntness Effects on the Stability Derivatives of Slender Cones in Hypersonic Flow," *Transactions of the Second Technical Workshop on Dynamic Stability Testing*, Paper 8, Vol. 1, Arnold Air Force Station, Tenn., 1965.

[5] Ericsson, L. E., "Unsteady Aerodynamics of an Ablating Flared Body of Revolution Including Effect of Entropy Gradient," *AIAA Journal*, Vol. 6, No. 12, Dec. 1968, pp. 2395–2401.

[6] Ericsson, L. E., "$\dot{\alpha}$-Effects are Negligible in Hypersonic Unsteady Flow—Fact or Fiction?" 19th International Astronautical Congress, New York, Oct. 13–19, 1968.

[7] Ericsson, L. E. and Scholnick, I. M., "Effect of Nose Bluntness on the Hypersonic Unsteady Aerodynamics of Flared and Conical Bodies of Revolution," AIAA Paper 68-889, Pasadena, Calif., 1968.

[8] Seiff, A., "Secondary Flow Fields Embedded in Hypersonic Shock Layers," TND-1304, May 1962, NASA.

[9] Ericsson, L. E. and Reding, J. P., "Dynamic Stability Problems Associated with Flare Stabilizers and Flap Controls," AIAA Paper 69-182, New York, 1969.

[10] Ericsson, L. E., "Effect of Boundary Layer Transition on Vehicle Dynamics," AIAA Paper 69-106, New York, 1969.

[11] Clay, J. T., "Nose Bluntness, Cone Angle, and Mach Number Effects on the Stability Derivatives of Slender Cones," ARL 57-0185, Sept. 1967, Aerospace Research Labs.

[12] Ward, L. K., "Influence of Boundary-Layer Transition on Dynamic Stability at Hypersonic Speeds," *Transactions of the Second Technical Workshop on Dynamic Stability Testing*, Paper 6, Vol. II, Arnold Air Force Station, Tennessee, April 20–22, 1965.

[13] Cleary, J. W., "Effects of Angle of Attack and Nose-Bluntness on the Hypersonic Flow over Cones," AIAA Paper 66-414, Los Angeles, Calif., 1966.

[14] Ericsson, L. E., "Effect of Nose Bluntness on the Hypersonic Unsteady Aerodynamics of an Ablating Re-Entry Body," *Journal of Spacecraft and Rockets*, Vol. 4, No. 6, June 1967, pp. 811–813.

[15] Jecmen, D. M., Reding, J. P., and Ericsson, L. E., "An Application of Automatic Carpet Plotting to Wind-Tunnel Data Reduction," *Journal of Spacecraft and Rockets*, Vol. 5, No. 3, March 1967, pp. 408–410.

DECEMBER 1969 AIAA JOURNAL VOL. 7, NO. 12

Acoustic Technique for Detection of Flow Transition on Hypersonic Re-Entry Vehicles

HANNO H. HELLER*
Bolt Beranek and Newman Inc., Cambridge, Mass.

This paper describes the development of an acoustic flow-transition detector for use on hypersonic ablating re-entry vehicles. The acoustic sensor of this system is recessed from the heat-shield surface and thus is protected from the externally developed heat; the sensor communicates with the external pressure field via a small-diameter vent. Results of supersonic wind-tunnel tests are presented which compare the characteristics of signals of an experimental transition detector with those of reference sensors (hot-wire probe, flush-mounted microphone) in transitional and fully developed turbulent flow.

I. Introduction and Summary

A. Statement of the Problem

ACCURATE determination of the time and location of flow transition on hypersonic, ablating, re-entry vehicles is very important for the successful planning and operation of a re-entry mission. Because of the excessive heat development on the surface of the re-entering vehicle, a direct measurement of flow transition by means of surface-mounted sensors is not feasible. Any such sensor would be quickly destroyed. The occurrence of flow transition is therefore usually inferred from data information not directly related to the flow phenomenon, e.g., from the increase of interior vibration levels.

This paper describes the development of an acoustic flow-transition detector system that senses fluctuating pressures directly on the surface of the ablating heat shield. This system makes use of a $\frac{1}{4}$-in.-diam piezo-electric microphone recessed from the surface and communicating with the fluctuating pressure field at the surface via a "probe tube" hole (Fig. 1).

It had been expected originally that a recessed microphone in contact with the surface pressure field would require elaborate thermal protection to assure no damage during the re-entry phase. Accordingly, an earlier developed acoustic system[1] for measuring surface pressure fluctuations involved a rather complicated arrangement of tubes and cavities preceding the microphone. Later arc tests,[2] however,

Received January 20, 1969; revision received June 6, 1969. The author wants to thank E. E. Ungar and R. H. Lyon of Bolt Beranek and Newman Inc. for many helpful discussions. The cooperation of R. H. Myers of Avco is also greatly appreciated. This work was accomplished under a subcontract from Avco Missile Systems Division and was sponsored by the Space and Missile Systems Organization, Norton Air Force Base, Calif. Thanks are due both of these organizations.

* Senior Engineering Scientist, Applied Physics Department.